# Efficient Jumpgliding: Theory and Design Considerations

Alexis Lussier Desbiens, Morgan Pope, Forrest Berg, Zhi Ern Teoh, Julia Lee, Mark Cutkosky

***Abstract*— A dynamic model of a jump glider is presented and correlated with the results obtained with a prototype glider. The glider uses a carbon fiber spring and a main wing that pivots approximately parallel to the airflow during ascent and latches into place for a gliding descent. The robot demonstrates longer traveled distance than an equivalent drag-free ballistic mass. A detailed numerical and a simplified algebraic model are also introduced, which are useful for exploring design tradeoffs and performance. These models suggest ways to improve the traveled distance and indicate that with modest variations in the wing angle of attack during ascent, one can choose from a variety of launch angles to accommodate variations in ground friction without greatly compromising range.**

## I. Introduction

Jumping has long been recognized as an effective form of locomotion for animals and robots that need to clear large obstacles relative to body size. It is particularly effective at small length scales, where the inherent strength/weight ratio is high. Many successful jumping robots have been demonstrated and a number of papers have focused on the problem of maximizing energy storage and efficiently converting stored elastic energy to kinetic energy for impressive performance [1]–[10]. Several groups have also added added deployable surfaces [11], [12] or fixed wings [13], [14] for improved range and control.

In nature, animals like the flying squirrel [15], the flying snake [16], and the flying fish [17] use aerodynamic surfaces on their bodies to dramatically extend the range and accuracy of their leaps, particularly when jumping from elevated perches.

In comparison to a ballistic jumper, adding the ability to glide can offer several advantages including:

- extended horizontal range for a given amount of stored energy
- greater control over the details of the trajectory (e.g. to allow a higher launch angle on slippery surfaces)
- a gentler landing.

However, the ability to achieve these benefits depends critically on how much extra weight and drag are associated with the controllable airfoil surfaces.

The contribution of this paper is to examine in detail the interrelationships among stored energy, lift, drag and trajectory control for efficient jump gliding with a glider that utilizes a pivoting wing. Section II presents the jump glider design, including the pivotable wing and carbon fiber bow spring. Section III presents a planar dynamic model of the glider. At the Reynolds numbers that apply for this prototype, a flat plate model of lift and drag is appropriate. The model elucidates the effects of friction at the wing pivot and the location of the center of mass of the wing. The results of experiments with the prototype are compared with predictions from the dynamic model and shown to match closely. However, for the purposes of exploring design tradeoffs, it is desirable to have a simpler, algebraic model for studying the effects of parametric variations. Such a model is introduced in Section IV and shown to match both the detailed model and empirical results reasonably well. Section V presents conclusions to be drawn from this work and future extensions to the models and jump glider design.

The authors are with the Biomimetics and Dextrous Manipulation Laboratory (BDML), Stanford University, Stanford, CA 94303, USA alexisld@alumni.stanford.edu, cutkosky@stanford.edu, mpope@stanford.edu

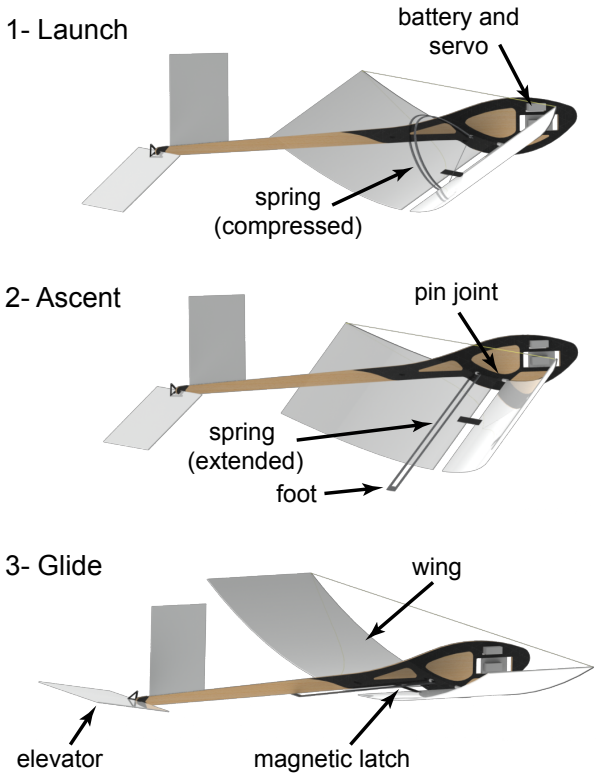


Fig. 1. Jump glider design with pivoting wing and carbon fiber spring, in the three principal states of a basic jump glide: launching, ascending, and gliding.

## II. Prototype

As noted in [18] for the study of jumping insects, the ratio of drag to inertial forces ($h_v A/m$) should be minimized for high efficiency during the ascending phase. In this equation, $h_v$ is the corresponding height of a jump in vacuum (related

to takeoff velocity), $A$ the exposed area of the body and $m$ the mass of the system. The jump-gliding plane presented here reduces the exposed wing area during ascent with a pivoting wing that can passively align itself with the air flow. The wing freely rotates for low drag during ascent but latches into place with a magnet to provide lift on descent. The plane is controlled using a single servo that adjusts the angle of the elevator. The following subsections describe the plane, the pivoting wing and the carbon fiber spring.

### A. Airplane and wing design

The airplane was designed to have a high glide ratio (i.e., high lift over drag, $L/D$) at the relatively low speeds achievable from jumping. For an airplane with a wingspan in the range of 0.5-1.0 m, flying at approximately 4 m/s, the Reynolds number is about 30,000. At these scales the maximum $L/D$ of a rectangular wing with an aspect ratio ($\mathcal{R}$) of 6 can be expected to be around 8-12 [19], [20]. The maximum $L/D$ ratio occurs at 3-4° of angle of attack (AoA) and at a lift coefficient of $C_L$=0.4. The same studies show that a rectangular planform (wing shape) with $\mathcal{R}$=6 performs better than a similar elliptical planform. Furthermore, a wing with $\mathcal{R}$=6 provides similar performance to a wing of higher aspect ratio without the practical disadvantages of a very long and slender wing. It was found that slightly better performance could be obtained with a 5% cambered plate. However, a flat wing was used in the present case for ease of manufacturing and damage repair.

To allow our 30g prototype to glide, the lift has to equal the gravity force, or $mg = 1/2\rho A v^2 C_L$. Solving for the wing area, $A$, and keeping the desired AR=6, the wing was sized to be 70 cm long with a cord of 11.5 cm. A thread is connected between the wing tips and pulls the wing into a slight upward bow (Fig 1), resulting in a slight dihedral angle for stability and reducing the tendency of the wing to bend excessively during the high acceleration associated with jumping.

The wing aerodynamical center (i.e. the quarter cord) is located just behind the center of mass (CM) of the airplane while gliding, while the elevator aerodynamical center is located 34 cm behind the CM. The elevator span is 14 cm and has a cord of 8 cm. This configuration allows the airplane to be longitudinally stable during gliding. The launch spring is connected to the airplane with a pivot at its center of mass, creating minimal angular acceleration and allowing for straight jumps at various angles.

The wing is built out of 1 mm thick Pro-formance™ foam with a leading edge carbon fiber spar. The round spar freely pivots within a styrene bushing attached to the body, allowing the wing to pivot. Lower friction could be achieved at this joint but is not needed, as will be shown in the following sections. Latching is accomplished at the end of the upward phase using two small magnets, one each on the wing and the body. The body is built out of balsa wood with 0.25 mm thick laser cut fiberglass FRP sheet for reinforcement. The airplane also has onboard a 90mAh LiPo battery and a 1.0g Micro 9-S-4CH receiver that controls a 2.5g Blue Arrow Servo connected to the elevator. The launch spring is currently manually loaded by pulling on a *Spectra* line, which is then cut by a heated nichrome wire for takeoff. This has proven to be sufficient to test jump-gliding capabilities and can be modified for autonomous operation in the future.

### B. Spring design

The main criteria considered when designing the jumping mechanism are the the mass of the foot, the force profile on the ground and the energy density of the spring mechanism. The mass of the foot should be minimized as it comes to a stop at the end of the decompression phase, dissipating kinetic energy in the process [2]. Equally important is the profile of the ground reaction force. Traditional linear springs have a triangular force profile that can cause premature lift-off and high initial accelerations that excite various structural modes. To overcome these limitations, one possibility is to employ a geared power transmission system [1], [2]. Another possibility is to use a bow spring providing a nearly constant force profile. The advantages of a carbon fiber bow spring for jumping have been noted previously [6]. Although a higher specific energy can be obtained with elastomers, a carbon fiber bow spring nonetheless provides a favorable energy density per mass, $\sigma_f^2/\rho E$ [21], without the deterioration over time of rubber.

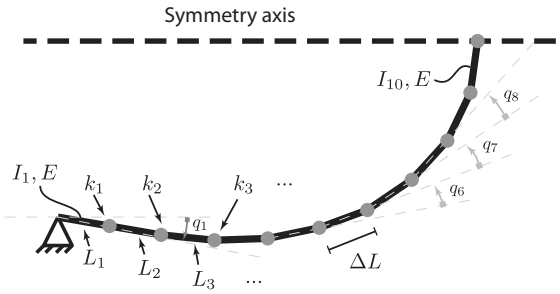


Fig. 2. Representation of half of the U-shaped carbon spring model used to size the spring.

The spring, which is bent into a U shape, is an elastica and can be approximated with a series of rigid elements connected by torsional springs of stiffness $k_i = EI_i/\Delta L$, where $I_i$ is the second moment of area and $\Delta L$ is the discretization length of each segment, as described in [22] and illustrated in Fig. 2. To find the angular displacements, $q_i$, when the tips are held a distance $L_{\text{compression}}$ apart, it suffices to minimize the potential energy:

$$\begin{aligned} \underset{q_i}{\text{minimize}} \quad & \frac{1}{2}\sum_{i=2}^{20} k_{i-1} q_i \\ \text{subject to} \quad & \mathbf{r}^{\text{end}/0} \cdot \hat{\mathbf{x}} = 0 \\ & \mathbf{r}^{\text{end}/0} \cdot \hat{\mathbf{y}} = L_{\text{compression}} \end{aligned}$$

This optimization problem can be solved using Lagrange multipliers. Once the angular displacements are found, the spring energy, tip forces, maximum bending moment and maximum stress are calculated.

The model suggests that to provide at least 0.53J, enough to propel a 30g airplane to a height of 1m with a forward velocity of 4m/s, one can use two unidirectional carbon fiber composite beams 15cm long, 3.8mm wide and 0.7mm thick. The Young's modulus of the composite was measured as 54GPa. When the distance between the tips of the spring is compressed to 5cm the stored energy is 0.63J. The maximum stress is 759MPa, only 38% of the 2GPa ultimate strength of the unidirectional carbon fiber. With a density of 1550 $\mathrm{kg/m^3}$, the spring mass is 1.2g.

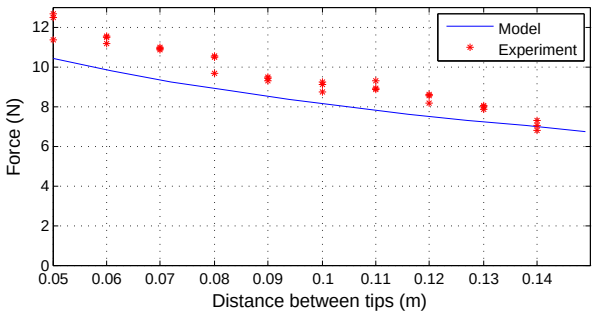


Fig. 3. Measured and predicted force as a function of the distance between the spring ends.

The static force profile of a prototype spring (10 mm wide instead of 7.6 mm) is illustrated in Fig. 3. The force profile is nearly constant with a force that varies from 6.8 to 10.4N. As described in [6], the force profile can be adjusted and the energy density optimized by varying the initial curvature and the second moment of inertia along the beam. Fig. 3 shows that the force measured in static tests trends as predicted by the model. The discrepancy is about 1.5 N, or 14%, and can be attributed mainly to the addition of some extra epoxy to prevent delamination with repeated tests. The predicted force is also quite sensitive to minor variations in the beam thickness.

Figure 5 plots the measured magnitude of the ground reaction force in the sagittal plane (non-sagittal forces are small and approximately zero mean) for three successive jumps at 45°launch angle. The forces were measured at 1000 samples per second from an ATI-Gamma SI-32-2.5 force/torque sensor and filtered with a tenth order zero-phase low-pass filter of degree ten and cut-off frequency of 100Hz to remove sensor noise. The peak dynamic force is slightly lower than the maximum static force, most likely a result of some foot slippage during takeoff. Note that the ground force magnitude remains above 6 N, or 2/3 of the peak force, for most of the ground contact phase.

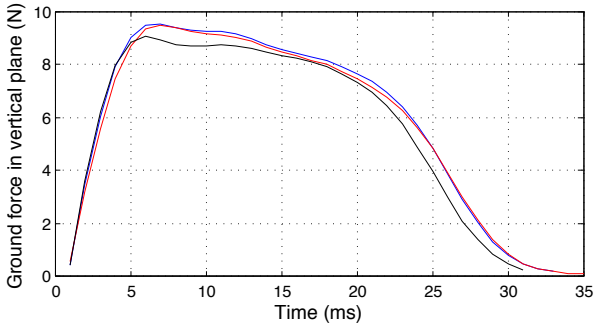


Fig. 5. Magnitude of the ground reaction force versus time for three launches of the aircraft from a force plate.

## III. Planar Dynamic Model

The model used to describe the behaviors of the jumpglider consists of two rigid bodies moving in a plane: the airframe and the wing. For convenience, a reference frame $\mathcal{A}$ is attached to the body. It is rotated with respect to the Newtonian reference frame $\mathcal{N}$ by an angle $q_A$ (pitch) around the unit vector $\hat{\mathbf{z}}_{\mathcal{N}}$. The reference frame $\mathcal{W}$ is attached to the wing, and is rotated with respect to $\mathcal{A}$ by an angle $q_W$ around $\hat{\mathbf{z}}_{\mathcal{A}}$. Using these definitions, one can represent the positions of the center of mass of the airframe, $\mathcal{A}_{\text{CM}}$, and the center of mass of the wing, $\mathcal{W}_{\text{CM}}$, as:

$$\mathbf{r}^{\mathcal{A}_{\text{CM}}/\mathcal{N}_0} = x\hat{\mathbf{x}}_{\mathcal{N}} + y\hat{\mathbf{y}}_{\mathcal{N}} \quad (1)$$

$$\mathbf{r}^{\mathcal{W}_{\text{CM}}/\mathcal{N}_0} = \mathbf{r}^{\mathcal{A}_{\text{CM}}/\mathcal{N}_0} + L_{\mathcal{P}/\mathcal{A}_{\text{CM}}}\hat{\mathbf{x}}_{\mathcal{A}} - L_{\mathcal{W}_{\text{CM}}/\mathcal{P}}\hat{\mathbf{x}}_{\mathcal{W}} \quad (2)$$

where $L_{\mathcal{P}/\mathcal{A}_{\text{CM}}}$ is the distance from $\mathcal{A}_{\text{CM}}$ to $\mathcal{P}$ along $\hat{\mathbf{x}}_{\mathcal{A}}$ and $L_{\mathcal{W}_{\text{CM}}/\mathcal{P}}$ is the distance from $\mathcal{P}$ to $\mathcal{W}_{\text{CM}}$ along $\hat{\mathbf{x}}_{\mathcal{W}}$.

The forces acting on the bodies include gravity on the airframe and the wing ($m_{\mathcal{A}}\mathbf{g}$ and $m_{\mathcal{W}}\mathbf{g}$ applied at their respective centers of mass), friction at the wing pivot point $\mathcal{P}$, and lift and drag on the wing, the elevator and the body. These forces are illustrated in Fig. 4.

As noted earlier, for the Reynolds numbers that apply to this jump glider, a flat plate model is appropriate to represent the lift $L$ and drag $D$ on the wing and elevator [23]:

$$L_i = \rho A_i ||^{\mathcal{N}}\mathbf{v}^{\text{AC}_i}||^2 \sin\alpha_i \cos\alpha_i \quad (3)$$

$$D_i = \rho A_i ||^{\mathcal{N}}\mathbf{v}^{\text{AC}_i}||^2 \sin^2\alpha \quad (4)$$

where $\rho$ is the air density and ${}^{\mathcal{N}}\mathbf{v}^{\text{AC}_i}$, $A_i$ and $\alpha_i$ are respectively the velocity of the aerodynamic center (AC) in reference frame $\mathcal{N}$, the area and the angle of attack of the aerodynamic surface $i$. In still air, $\alpha$ represents the angle between the velocity of the AC and the vector from the trailing edge to the leading edge. Drag opposes the velocity of the AC while lift is perpendicular to it. Both forces are applied at the quarter cord when measured from the leading edge. An additional parasitic drag force is modeled on the body ($D_{0_{\mathcal{A}}} = 1/2\rho A_{\mathcal{W}} ||^{\mathcal{N}}\mathbf{v}^{\mathcal{A}_{\text{CM}}}||^2 C_{D_0}$) and applied at the center of mass of the airplane.

Friction at the pivot is modeled as viscous damping and creates a torque of $\mathbf{T}_f = -b_{\mathcal{W}} q_{\mathcal{W}} \hat{\mathbf{z}}_{\mathcal{A}}$ on the wing. Viscous friction was chosen because of its simplicity in numerical simulation. Furthermore, because the wing pivots at a roughly constant angular velocity through the ballistic phase for jump angles between 30-65° a viscous term produces a similar effect to Coulomb friction. Moreover, the frictional torque is small compared to other terms.

At the apex of a jump, the wing latches into place for gliding. To simulate this effect, a stiff torsional spring and

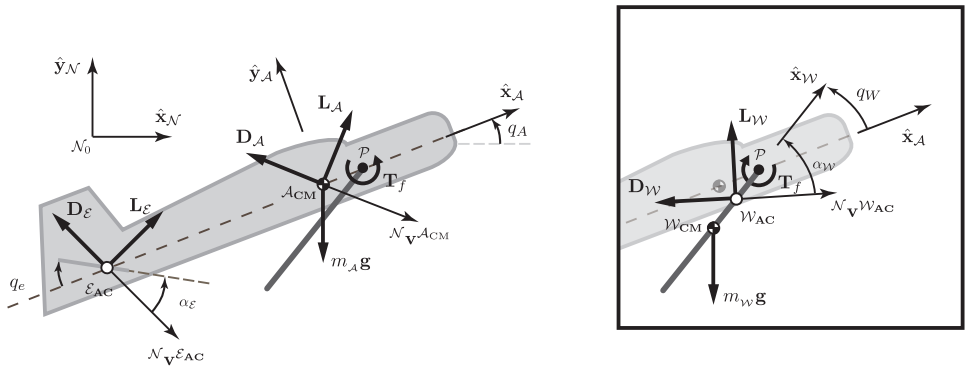


Fig. 4. Reference frames and forces on the plane body, wing, and elevator used in the detailed model. Left drawing highlights forces and moments on the body, right drawing highlights forces and moments on the wing. Reaction forces at the wing pivot ($\mathcal{P}$) not shown for simplicity.

damper are enabled when the absolute value of $q_{\mathcal{W}}$ is smaller than 2°. For simplicity, the spring-powered launch is approximated by specifying the initial velocity of the airplane at take-off.

The acceleration of the center of mass of each body $i$ in frame $\mathcal{N}$ is obtained by differentiating its position twice with respect to time in reference frame $\mathcal{N}$ and is denoted as ${}^{\mathcal{N}}\mathbf{a}^{i_{\mathrm{CM}}}$. The angular velocity and acceleration of a body $i$ in reference frame $\mathcal{N}$ are respectively denoted as ${}^{\mathcal{N}}\boldsymbol{\omega}^i$ and ${}^{\mathcal{N}}\boldsymbol{\alpha}^i$. Following a D'Alembert approach, the sums of the forces and moments on the system are equated to the sums of the inertial and other dynamic terms, referred to as the effective forces and effective moments [24].

The three resulting vector equations consist of the sum of forces on the system ($\mathbf{F}^{\mathcal{S}}$) equated to the sum of effective forces (Eq. 5), the sum of moments around the airplane center of mass ($\mathbf{M}^{\mathcal{S}/\mathcal{A}_{\mathrm{CM}}}$) equated to the sum of the effective moments of the system around the same point (Eq. 6), and the sum of moments on the wing around the pivot ($\mathbf{M}^{\mathcal{W}/\mathcal{P}}$) equated with the effective moment of the wing around that point (Eq. 7).

$$\mathbf{F}^{\mathcal{S}} = (m_{\mathcal{A}} + m_{\mathcal{W}}) * ({}^{\mathcal{N}}\mathbf{a}^{\mathcal{A}_{\mathrm{CM}}} + {}^{\mathcal{N}}\mathbf{a}^{\mathcal{A}_{\mathrm{CM}}}) \quad (5)$$

$$\mathbf{M}^{\mathcal{S}/\mathcal{A}_{\mathrm{CM}}} = \underline{\mathbf{I}}^{\mathcal{A}/\mathcal{A}_{\mathrm{CM}}} \cdot {}^{\mathcal{N}}\boldsymbol{\alpha}^{\mathcal{A}} + \underline{\mathbf{I}}^{\mathcal{W}/\mathcal{A}_{\mathrm{CM}}} \cdot {}^{\mathcal{N}}\boldsymbol{\alpha}^{\mathcal{W}} + \ldots \; m_{\mathcal{W}} * \mathbf{r}^{\mathcal{W}_{\mathrm{CM}}/\mathcal{A}_{\mathrm{CM}}} \times {}^{\mathcal{N}}\mathbf{a}^{\mathcal{A}_{\mathrm{CM}}} \quad (6)$$

$$\mathbf{M}^{\mathcal{W}/\mathcal{P}} = \underline{\mathbf{I}}^{\mathcal{W}/\mathcal{P}} \cdot {}^{\mathcal{N}}\boldsymbol{\alpha}^{\mathcal{W}} + m_{\mathcal{W}} * \mathbf{r}^{\mathcal{W}_{\mathrm{CM}}/\mathcal{P}} \times {}^{\mathcal{N}}\mathbf{a}^{\mathcal{P}} \quad (7)$$

Four scalar equations are obtained by taking the dot product of each side of these vector equations with respect to appropriate unit vectors. Eq. 5 is dotted with $\hat{\mathbf{x}}_{\mathcal{N}}$ and $\hat{\mathbf{y}}_{\mathcal{N}}$. Eq. 6 and 7 are dotted with $\hat{\mathbf{z}}_{\mathcal{N}}$. The resulting scalar equations are solved for $\ddot{x}$, $\ddot{y}$, $\ddot{q}_A$ and $\ddot{q}_W$. In the present case the solutions were obtained using Motion Genesis [25] and solved numerically in Matlab.

### A. Results

The airplane was launched at various angles and the trajectory recorded at 200 fps with a high speed camera. The elevator was manually controlled by first aligning it with the launch angle to minimize drag on the way up and then flipped to its trimmed position for gliding as the airplane reached its apex. Figure 6 shows a typical flight for a launch angle of 60°.

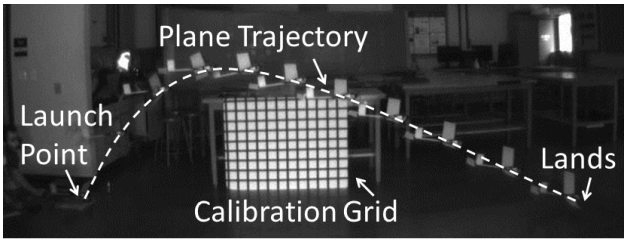


Fig. 6. Typical jumpgliding trajectory for the jump glider. Each image is spaced by 150ms.

The camera was calibrated to compensate for distortion and the center of mass position was tracked in each frame. The resulting position was filtered by fitting a $12^{\text{th}}$ order polynomial. The high degree was necessary to accommodate the change from ballistic motion to gliding. The polynomial was then differentiated to obtain the velocity. The energy level was calculated by adding potential and kinetic energies. Results are illustrated in Figs. 7-9.

The model parameters used in these figures are: wing

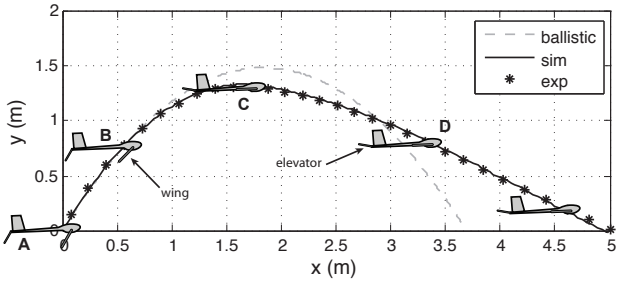


Fig. 7. Comparison of the experimental trajectory, the simulated trajectory and a ballistic trajectory with the same energy and launch angle (58°). Overlaid on that figure are cartoons of the jump glider states. The wing and elevator are initially aligned with the launch angle (**A**). During the upward phase, the wing freely rotates to stay aligned with the airflow (**B**). At the apex (**C**), the wing reaches a horizontal orientation and latches to the body while the elevator is moved up to its gliding position. The wing and elevator remain in that configuration for the full glide phase (**D**).

area of $0.0805\mathrm{m}^2$, elevator area of $0.0112\mathrm{m}^2$, body area of $1.5\times10^{-5}\mathrm{m}^2$, $C_{D_0}$ of 0.01, zero joint friction, body mass of 23.8g, wing mass of 6.2g, body inertia around its center of mass of $3.0\times10^{-4}\mathrm{kgm}^2$ and wing inertia around its center of mass of $1.5\times10^{-5}\mathrm{kgm}^2$. In simulation, the elevator was oriented with the flow on the way up and switched to an angle of 7.5° (upward) as the wing latched in place for gliding.

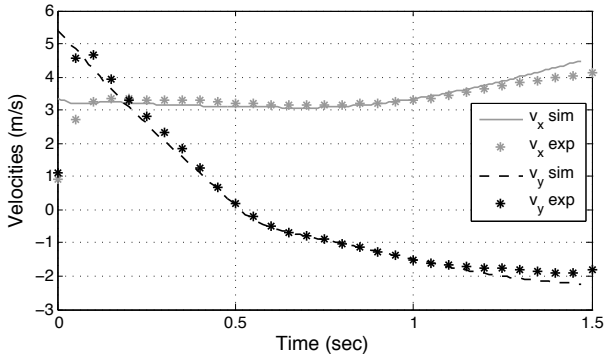


Fig. 8. Comparison of experimental and simulated velocities during jump gliding. The transition from ballistic motion to gliding happens at 0.6s.

As seen in Fig. 7 the model fits the experimental trajectory during the ballistic and glide phases. The airplane does not go as high as a drag-free ballistic trajectory with the same launch angle (58°) because of body drag. Nonetheless, it travels 40% further than the drag-free ballistic trajectory. The distance is also 20% longer than the distance for a drag-free ballistic trajectory with an ideal 45° launch angle (4.11m). Note also that a 45° launch angle could be difficult to achieve as it requires a coefficient of friction greater than one.

The velocities (Fig. 8) also show good agreement with the model. The first phase ($t < 0.6\mathrm{s}$) is essentially ballistic while the second phase sees an increasing horizontal and (negative) vertical velocity. This indicates that the elevator trim could be increased to get a better, shallower glide.

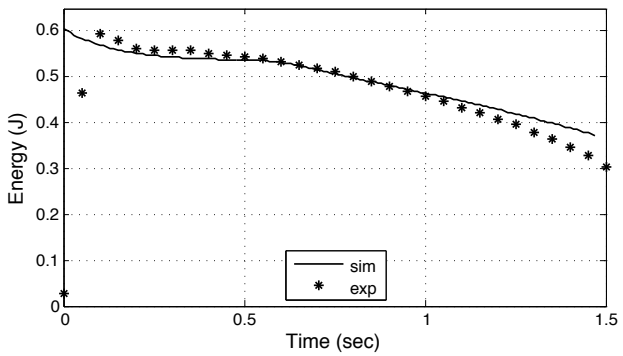


Fig. 9. Comparison of experimental and simulated energy level during jump gliding.

The energy of the system (Fig. 9) is almost constant during the ballistic phase, except for an initial drop caused by the body drag at the high initial velocity. During the second phase, the energy reduces slowly due to drag while gliding.

### B. Influence of pivot friction

Friction at the wing pivot causes the angle of attack ($\alpha$) to be non-zero during the first phase, creating some additional lift and drag. However, for a small angle of attack lift is proportional to $\alpha$ and the drag is proportional to $\alpha^2$. Thus, lift is the dominant force. In still air, lift is a conservative force because it is orthogonal to the instantaneous direction of motion. It changes the shape of the trajectory but not the energy available to the glider. Small amounts of lift caused by friction at the pivot affect the trajectory of the airplane by slowing its forward velocity but simultaneously increasing the height of the apex.

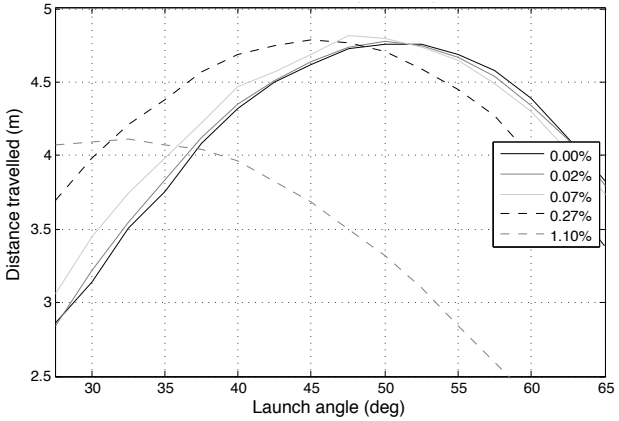


Fig. 10. For small amounts of pivot friction, the maximum distance traveled is not affected but the launch angle should be reduced to compensate for the lift created. The different curves correspond to varying amounts of average pivot friction expressed as a percentage of the maximum torque on the wing due to gravity. For the glider prototype the pivot friction is approximately 0.07% of the maximum torque on the wing due to gravity.

To investigate how these changes in trajectory affect the total distance, a glide controller acting on the elevator was added to maintain the forward velocity that was experienced at the apex for the duration of the glide. Simulations were performed for different combinations of launch angles and friction at the wing pivot. The results are illustrated in Fig. 10. For a frictionless pivot, the jump angle allowing the airplane to reach the maximum glide distance is around 52°. As friction increases, the optimum jump angle is reduced, due to the lift contribution, but the distance traveled remains nearly constant. This insensitivity to modest amounts of pivot friction motivates the choice of a passive solution for varying wing angle, as adopted in the prototype.

### C. Implications of Lift During Ascent Phase

The previous discussion of the effect of friction at the pivot raises the point that small amounts of lift can be used to alter the trajectory without sacrificing significant energy due to increased drag. Thus by using the wing of the jump glider as a control surface, one can achieve peak heights and forward velocities optimal for gliding under a range of take-off angles. This is particularly important considering that a jump at 40° requires a ground coefficient of friction of at least 1.19 while a jump at 60° requires a more reasonable

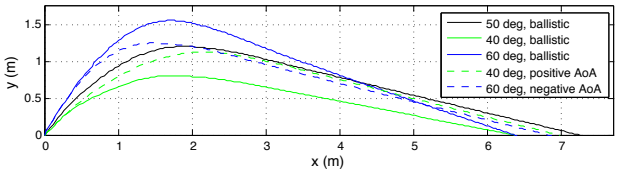


Fig. 11. Influence of lift during the ascending phase. Solid lines represent launches with zero lift. However, with positive lift at 40° or negative lift at 60°, the range is extended.

coefficient of 0.57. As Fig. 11 illustrates, both the 40° and the 60° launches reduce the total travelled distance by about one meter (14%) when compared to a 50° launch. By using *negative* lift during the ascent one can recover the lost distance for a jump at 60°. Conversely, if takeoff conditions favor a lower launch angle, one can use positive lift for a launch angle of 40°.

### D. Influence of wing's CM and AC

The influence of the position of the wing center of mass and aerodynamical center on the ascending portion of the flight can be understood by expanding Eq. 7. In this equation, the sum of moments can be written as:

$$\mathbf{M}^{\mathcal{W}/\mathcal{P}} = \mathbf{r}^{\mathcal{W}_{\text{CM}}/\mathcal{P}} \times m_{\mathcal{W}}\mathbf{g} + \mathbf{r}^{\mathcal{W}_{\text{AC}}/\mathcal{P}} \times \mathbf{L}_{\mathcal{W}} - b\dot{q}_{\mathcal{W}}\hat{\mathbf{z}}_{\mathcal{N}} \quad (8)$$

Note that in this equation the drag is ignored as, for small angles of attack, it is negligible compared to the lift force. Furthermore, shortly after takeoff the wing angular velocity, ${}^{\mathcal{N}}\boldsymbol{\omega}^{\mathcal{W}}$, reaches an almost constant rotation rate to remain aligned with the flow. As the angular velocity is constant, the angular acceleration of the wing, ${}^{\mathcal{N}}\boldsymbol{\alpha}^{\mathcal{W}}$, will be close to zero, eliminating the first term on the left side of Eq. 7. Combining Eq. 8 with the simplified version of Eq. 7, one obtains:

$$0 = \mathbf{r}^{\mathcal{W}_{\text{CM}}/\mathcal{P}} \times m_{\mathcal{W}}(\mathbf{g} - {}^{\mathcal{N}}\mathbf{a}^{\mathcal{P}}) + \mathbf{r}^{\mathcal{W}_{\text{AC}}/\mathcal{P}} \times \mathbf{L}_{\mathcal{W}} - b\dot{q}_{\mathcal{W}}\hat{\mathbf{z}}_{\mathcal{N}} \quad (9)$$

For ideal conditions with negligible friction, $b$, at the wing's pivot, very little lift, $\mathbf{L}_{\mathcal{W}}$, needs to be generated to balance this equation. With low amounts of lift, the acceleration of the wing's rotation point, ${}^{\mathcal{N}}\mathbf{a}^{\mathcal{P}}$, is comparable to the gravitational acceleration. In this case, the position of the wing center of mass with respect to the rotation point, $\mathbf{r}^{\mathcal{W}_{\text{CM}}/\mathcal{P}}$, is not particularly important as $\mathbf{g}$ and ${}^{\mathcal{N}}\mathbf{a}^{\mathcal{P}}$ cancel each other. This is the case for the glider presented in this paper.

When friction at the wing pivot cannot be ignored, some lift will be created to compensate for the moment created by friction. This lift force changes the acceleration of the rotation point and the term $(\mathbf{g} - {}^{\mathcal{N}}\mathbf{a}^{\mathcal{P}})$ becomes non-negligible. In this case, the wing's center of mass and aerodynamical center positions become important design parameters.

## IV. A Simplified Model for Design Exploration

The model described in the previous section answers some questions about the behavior of a jump glider. However it requires numerical computations for every tested case. More importantly, the model doesn't naturally distill the intent of a perfect jump glide. Thus, any poor design choices (e.g. in the airframe or in the gliding controller) will allow the numerical model to suggest suboptimal performance.

A simplified model was therefore developed to more readily answer such questions as:

1) What is the maximum jump gliding distance?
2) What is the optimum jump angle, initial velocity and starting jump height?
3) What are the most important design parameters?

The simplified model decomposes the flight into three distinct phases: an initial ballistic phase up to the apex, a transitional phase to reach the required gliding conditions and a final gliding phase. This simplified model can be thought of as a template for use with any controller implemented on the airplane and by the designer to identify the best possible performances. The following subsections describe the simplified model by calculating the horizontal ($\Delta x$) and vertical ($\Delta y$) distances traveled in each phase.

### A. Ballistic phase

The first phase involves a typical ballistic trajectory. It assumes that the wing, body and elevator create negligible lift and drag. Under these conditions, and for an initial velocity $v$ and jump angle $\theta$, the distances traveled are:

$$\Delta y_B = \frac{v^2 \sin^2(\theta)}{2g} \ , \ \Delta x_B = \frac{v^2 \sin(\theta)\cos(\theta)}{g} \quad (10)$$

While this simplification would seem to preclude strategies like using positive or negative lift as discussed in the previous section, the point is that such strategies involve small amounts of lift and drag and do not substantially affect the selection of airframe design parameters or traveled distance.

### B. Transition

Adding a transition phase provides a better estimate of the overall gliding distance, which will be underestimated if it is assumed that the airplane commences gliding at the apex. The underestimation arises because the plane continues to accelerate along an almost ballistic trajectory until its downward velocity matches the velocity required for gliding. The vertical gliding velocity depends on the forward velocity imparted initially by the jump and on the parameters defining the airplane. To solve for the vertical velocity at which the transition occurs, one can use the lift to drag ratio, $L/D$, for flat plates at small angles of attack:

$$\frac{L}{D} = -\frac{v_x}{v_y} = \frac{mg}{\frac{m^2 g^2}{A\rho v^2} + \frac{1}{2}A\rho C_{D_0} v^2} \quad (11)$$

This equation is unfortunately difficult to solve for $v_y$ as it implies a fifth order equation in $v_x$. Furthermore, it is derived for a small angle of attack, or large $L/D$ ratio, when the forward velocity is high compared to the vertical velocity. This condition is hard to achieve for most small jumpers due to the difficulty in storing enough energy in the spring and achieving high $L/D$ at small scale.

A more suitable approach in this case is to use a linear approximation between a free fall glide ($L/D = 0, v_x = 0$)

and a glide at the maximum $L/D$. Differentiating Eq. 11 with respect to the velocity $v$ and equating to zero, one can find the velocity at maximum lift to drag ratio and the value of the maximum:

$$v^2_{(L/D)_{\max}} = \frac{mg}{\rho A}\sqrt{\frac{2}{C_{D_0}}}\ ,\ (L/D)_{\max} = \sqrt{\frac{1}{2C_{D_0}}}. \quad (12)$$

Assuming that the forward velocity $v_x$ at maximum $L/D$ are approximately equal to $v_{(L/D)_{\max}}$, and knowing that $L/D$ is equal to zero at zero forward velocity, one can approximate the relationship between the lift to drag ratio and the forward velocity as linear for $v_x < v_{(L/D)_{\max}}$:

$$\frac{L}{D} \approx \frac{(L/D)_{\max}}{v_{(L/D)_{\max}}} v_x = -\frac{1}{v_{y_G}} v_x \quad (13)$$

where the constant parameter $v_{y_G}$ is defined as:

$$v_{y_G} = -\sqrt{\frac{mg}{\rho A}}\left(8C_{D_0}\right)^{1/4}. \quad (14)$$

Using the preceding equations, the end of the transition phase can be determined by equating the vertical velocity during the ballistic transition phase to the vertical velocity required to start gliding (i.e., $v_{y_G}$). With the end of the transition phase known, it is possible to solve for the distance:

$$\Delta x_T = -\frac{v_{y_G}}{g} v\cos\theta\ ,\ \Delta y_T = \frac{1}{2g} v^2_{y_G} \quad (15)$$

### C. Gliding

Once the transition phase is over and the vertical velocity is suitable for gliding, the airplane maintains a constant glide slope determined by the $L/D$ ratio. The distance during this phase is:

$$\begin{aligned} \Delta x_G &= \frac{L}{D}(\Delta y_B - \Delta y_T + \Delta h) \\ &= -\frac{v\cos\theta}{v_{y_G}}\left(\frac{v^2\sin^2(\theta)}{2g} - \frac{v^2_{y_G}}{2g} + \Delta h\right) \end{aligned} \quad (16)$$

where $\Delta h$ is the height drop between the start and finish point.

### D. Results

With each phase defined, it is possible to calculate the total distance travelled:

$$\begin{aligned} \Delta x &= \Delta x_B + \Delta x_T + \Delta x_G \\ &= \frac{v^2\sin\theta\cos\theta}{g} - \frac{v_{y_G}}{2g} v\cos\theta ... \\ &\quad -\frac{v^3\sin^2\theta\cos\theta}{2g v_{y_G}} - \frac{v\cos\theta}{v_{y_G}}\Delta h \end{aligned} \quad (17)$$

Under normal conditions, all terms of this equation are positive as $v_{y_G}$ is negative. Furthermore, even when only a small lift to drag ratio is obtained by the gliding platform, the second term will be small compared to the others.

We can now return to the three questions posed at the beginning of this section. In answer to questions 1 and 2, for a fixed airplane design (i.e. fixed $v_{y_G}$), it is possible to describe the evolution of the optimal jump angle as the jump parameters $v$, $\theta$ and $\Delta h$ are varied by looking at Eq. 17. The first term of this equation favors a 45° jump angle (due to $\sin\theta\cos\theta$), the third term favors a jump angle around 54° ($\sin^2\theta\cos\theta$) and the last term favors a horizontal jump ($\cos\theta$). Each of these terms has a different importance as $v$ and $\Delta h$ are varied. The third term can be dominant at higher launch speeds while the last term becomes dominant for larger drops between the start and finish vertical positions. This effect can be seen in Figs. 12 -13. The optimal jump angle on a flat surface is 50-52° but reduces to 45° when the drop height increases to 1 m.

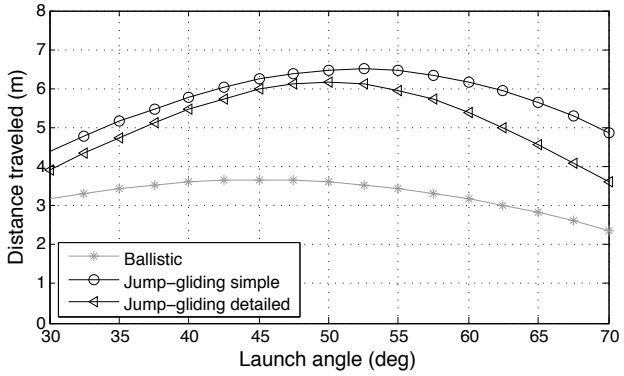


Fig. 12. $h_0$ = 0 m and $v_0$ = 6 m/s

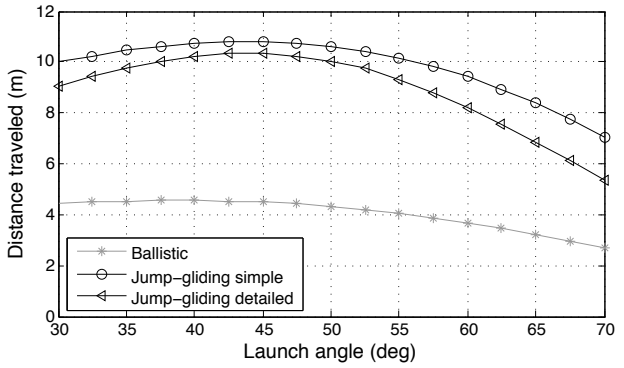


Fig. 13. $h_0$ = 1 m and $v_0$ = 6 m/s

In partial answer to question 3, we see that the distance is also affected by the airplane design. To increase it, the parameter $v_{y_G}$ (Eq. 14) should be brought toward zero, which means that the mass to lifting surface area ratio should be decreased, along with the parasitic drag coefficient.

Figures 12 and 13 also reveal that the simplified model over-predicts the traveled distance when compared to the detailed model. This is because the full wing area is used in Eq. 14 and, due to the design of the plane, the elevator has to create some negative lift to maintain the required moment balance during gliding. This reduces the effective surface area responsible for creating lift. The area used by the simpler model could be reduced to reflect this effect. Even better, the airplane could be redesigned so that the elevator creates negligible or positive lift while gliding.

Another difference is that the distance traveled in Fig. 7 is smaller than predicted by both the detailed model and the simplified model in Fig. 12. The reason is that the results from the detailed model in Fig. 12 were computed for zero body area for purposes of comparison with the simplified model. The effect of body area can be seen in Fig. 7 when comparing the height reached by the ballistic trajectory and the height reached by the experimental trajectory. It is also seen as the initial energy drops in Fig. 9. This change of trajectory cannot be attributed to the pivot friction, which would keep the energy nearly constant, as discussed in Section III-B. The models suggest that reducing the body drag would allow the airplane to travel between 0.5-1.2$\mathrm{m}$ farther. The current jump glider already travels further than an equivalent drag free point mass launched at 45°. An appropriate next benchmark would be traveling a longer horizontal distance than a lighter, wingless jumping robot with the same initial energy, which could be accomplished through reduced body drag (and/or reduced wing mass, better control of the glide, improved $L/D$ with wing curvature and reduced wing mid section gap, or positive lift on the elevator). The current jump glider travels 5.01$\mathrm{m}$ while a 23.8$\mathrm{g}$ ballistic jumper with 0.60J of energy would travel 5.18$\mathrm{m}$ when launched at 45°, assuming that there is enough friction at the foot to do so.

## V. Conclusions and Future Work

This paper verifies the intuitive conclusion that gliding can increase the horizontal range of a jumping robot. The presented models provide additional insight into the benefits of controllable aerodynamic surfaces. For example, during the upward ballistic phase, lift can be used to control the apex height and forward velocity from a range of launch angles without sacrificing significant energy in drag. As a consequence, it is possible to choose a steeper launch angle on a slippery surface without significantly reducing range. In addition, in all phases of the maneuver, the aircraft can benefit from the increased controllability offered by its wings without suffering significantly from increased drag.

More generally, the models provide insight regarding the effects of various design parameters on jump gliding performance – for example, to explore the merits of a more complex wing folding mechanism that reduces drag at the expense of greater weight, or to evaluate the improvement possible with a reduced body area.

Looking forward, improvements can be made to the launching spring and platform design, but the main extension will be to provide greater control during flight (e.g. to steer around obstacles or to optimize the glide path), particularly when jumping from a height.

## References


[1] M. Kovac, M. Fuchs, A. Guignard, J. Zufferey, and D. Floreano, "A miniature 7g jumping robot," in *IEEE International Conference on Robotics and Automation*, 2008, pp. 373–378.

[2] J. Burdick and P. Fiorini, "Minimalist jumping robots for celestial exploration," *The International Journal of Robotics Research*, vol. 22, no. 7-8, p. 653, 2003.

[3] P. Weiss, "Hop… hop… hopbots!: Designers of small, mobile robots take cues from grasshoppers and frogs," *Science News*, vol. 159, no. 6, pp. 88–91, 2001.

[4] E. Ackerman, "Boston dynamics sand flea robot demonstrates astonishing jumping skills," *IEEE Spectrum*, March 2012.

[5] U. Scarfogliero, C. Stefanini, and P. Dario, "The use of compliant joints and elastic energy storage in bio-inspired legged robots," *Mechanism and Machine Theory*, vol. 44, no. 3, pp. 580–590, 2009.

[6] G. Zeglin, "The bow leg hopping robot," Ph.D. dissertation, Carnegie Mellon University, 1999.

[7] B. Lambrecht, A. Horchler, and R. Quinn, "A Small, Insect-Inspired Robot that Runs and Jumps," in *IEEE International Conference on Robotics and Automation*, 2005, pp. 1240–1245.

[8] H. Tsukagoshi, M. Sasaki, A. Kitagawa, and T. Tanaka, "Jumping robot for rescue operation with excellent traverse ability," in *12th International Conference on Advanced Robotics*, 2005, pp. 841–848.

[9] M. Wang, X.-z. Zang, J.-z. Fan, and J. Zhao, "Biological Jumping Mechanism Analysis and Modeling for Frog Robot," *Journal of Bionic Engineering*, vol. 5, no. 3, pp. 181–188, Sep. 2008.

[10] A. Yamada, M. Watari, H. Mochiyama, and H. Fujimoto, "An asymmetric robotic catapult based on the closed elastica for jumping robot," in *IEEE International Conference on Robotics and Automation*, May 2008, pp. 232–237.

[11] M. A. Woodward and M. Sitti, "Design of a miniature integrated multi-modal jumping and gliding robot," *International Conference on Intelligent Robots and Systems*, 2011.

[12] R. Armour, K. Paskins, A. Bowyer, J. Vincent, and W. Megill, "Jumping robots: a biomimetic solution to locomotion across rough terrain," *Bioinspiration & Biomimetics*, vol. 2, p. S65, 2007.

[13] M. Kovac, "Bioinspired jumping locomotion for miniature robotics," Ph.D. dissertation, Ecole Polytechnique Fédérale de Lausanne, 2010.

[14] M. Kovac, W. Hraiz, O. Fauria, J. Zufferey, and D. Floreano, "The epfl jumpglider: A hybrid jumping and gliding robot with rigid or folding wings," in *IEEE International Conference on Robotics and Biomimetics (ROBIO)*, 2011, pp. 1503–1508.

[15] K. Vernes, "Gliding Performance of the Northern Flying Squirrel ( Glaucomys Sabrinus ) in Mature Mixed Forest of Eastern Canada," *Journal of Mammalogy*, vol. 82, no. 4, pp. 1026–1033, Nov. 2001.

[16] J. Davenport, "How and why do flying fish fly?" *Reviews in Fish Biology and Fisheries*, vol. 4, no. 2, pp. 184–214, Jun. 1994.

[17] J. J. Socha, "Becoming airborne without legs: the kinematics of take-off in a flying snake, Chrysopelea paradisi." *The Journal of experimental biology*, vol. 209, Sep. 2006.

[18] H. Bennet-Clark and G. Alder, "The effect of air resistance on the jumping performance of insects," *Journal of Experimental Biology*, vol. 82, no. 1, p. 105, 1979.

[19] A. Pelletier and T. Mueller, "Low reynolds number aerodynamics of low-aspect-ratio, thin/flat/cambered-plate wings," *Journal of Aircraft*, vol. 37, no. 5, pp. 825–832, 2000.

[20] E. Laitone, "Wind tunnel tests of wings and rings at low reynolds numbers." *Progress in Astronautics and Aeronautics*, vol. 195, pp. 83–90, 2001.

[21] M. Ashby and M. Ashby, *Materials selection in mechanical design*. Cambridge Univ Press, 2005, vol. 519.

[22] L. Howell, *Compliant mechanisms*. Wiley-Interscience, 2001.

[23] R. Cory and R. Tedrake, "Experiments in fixed-wing uav perching," in *Proceedings of the AIAA Guidance, Navigation, and Control Conference*, 2008.

[24] T. Kane and D. Levinson, *Dynamics, theory and applications*. McGraw Hill, 1985.

[25] Motion Genesis, "Motion Genesis™," 2010. [Online]. Available: http://www.motiongenesis.com/